

ON THE INTERACTION BETWEEN CONVECTION AND MAGNETIC FIELDS

FAUSTO CATTANEO

Department of Mathematics, University of Chicago, 5734 South University Avenue, Chicago, IL 60637;
cattaneo@math.uchicago.edu

THIERRY ÉMONET

Department of Astronomy and Astrophysics, University of Chicago, 5640 South Ellis Avenue, Chicago, IL 60637;
emonet@flash.uchicago.edu

AND

NIGEL WEISS

Department of Applied Mathematics and Theoretical Physics, University of Cambridge, Cambridge CB3 9EW, UK;
n.o.weiss@damtp.cam.ac.uk

Received 2002 November 11; accepted 2003 January 20

ABSTRACT

Turbulent convection in the solar photosphere can act as a small-scale dynamo, maintaining a disordered magnetic field that is locally intense. On the other hand, convection is inhibited in the presence of a strong, externally imposed magnetic field, as for instance, in a sunspot. Large-scale, three-dimensional, numerical experiments on highly nonlinear magnetoconvection in a Boussinesq fluid show that there is a continuous transition from a dynamo regime through a convective regime to an oscillatory regime as the strength of the imposed magnetic field is progressively increased. The patterns found in these different regimes are described and analyzed.

Subject headings: convection — Sun: magnetic fields — Sun: photosphere

1. INTRODUCTION

Magnetic activity is exhibited by late-type stars with deep convective envelopes, but the fine structure of the magnetic field can only be detected on the Sun. Recent observations, from the ground and from space, are now revealing the intimate relationship between small-scale magnetic features in the solar atmosphere and convection on the scale of photospheric granulation (Title 2000). Meanwhile, the availability of powerful computers has made it possible to simulate the three-dimensional interplay between magnetic fields and convection (Cattaneo 1999; Weiss, Proctor, & Brownjohn 2002). The fields measured at the solar surface span a wide range of scales (Stix 2002). At one extreme are the large-scale fields associated with the solar cycle (including those in sunspots and active regions); it is widely accepted that they are generated by a deep-seated dynamo, in a region where convection is strongly influenced by rotation. In contrast, the quiet-Sun fields are disordered and constantly evolving. The Michelson Doppler Imager observations from *SOHO* show magnetic flux emerging in ephemeral active regions to form the so-called magnetic carpet and being swept into the supergranular network, while *G*-band images from La Palma reveal rapidly evolving fine-scale fields in intergranular lanes. Thus, it becomes important to model the local interactions between convection and magnetic fields in different regions, where the mean vertical field strength ranges from a high value (as in a sunspot) through moderate values (as in a plage) to the low values characteristic of the quiet Sun.

That large-scale stellar dynamos rely on the influence of rotation and dynamo action by convection in a rapidly rotating layer has previously been explored (Nordlund et al. 1992; Brandenburg et al. 1996). The influence of the Coriolis force on photospheric convection is, however, unimportant, since the turnover times of granules, mesogranules, and

supergranules are all much shorter than the Sun's rotation period. Nevertheless, small-scale disordered fields may be generated by local dynamo action near the photosphere (Cattaneo 1999). So far, numerical investigations of three-dimensional interactions between convection and magnetic fields have focused on either turbulent dynamos (Meneguzzi & Pouquet 1989; Cattaneo 1999; Thelen & Cattaneo 2000; Cattaneo, Lenz, & Weiss 2001; Emonet & Cattaneo 2001), magnetoconvection (see, e.g., Tao et al. 1998; Rucklidge et al. 2000; Weiss et al. 2002), or flux pumping (Tobias et al. 1998, 2001; Dorch & Nordlund 2001), regarded separately. In each case, it is essential to model vigorous, strongly nonlinear flows in sufficiently wide boxes.

Computational studies of magnetoconvection have followed two different but complementary approaches (Schüssler 2001). One school has attempted, with increasing success, to simulate the actual behavior on the Sun, including effects such as compressibility, ionization, and radiative transfer (see, e.g., Stein, Bercik, & Nordlund 2002; Stein & Nordlund 2003). The alternative approach (which we follow) is to construct idealized numerical experiments in order to isolate and understand the physical processes that are involved. It is certainly possible to investigate compressible magnetoconvection, but computational constraints then limit the degree of nonlinearity (as measured by a magnetic Reynolds number, R_m) that can be attained. So a thorough survey of the transition from turbulent magnetoconvection to dynamo action is still feasible only within the Boussinesq approximation.

This paper presents for the first time such a systematic survey at high magnetic Reynolds numbers of these turbulent interactions between magnetic fields and convection in a Boussinesq fluid, as the net magnetic flux through the box is increased from zero to a value great enough to halt convection. When no net field is imposed, convection acts as a dynamo, maintaining a small-scale turbulent magnetic

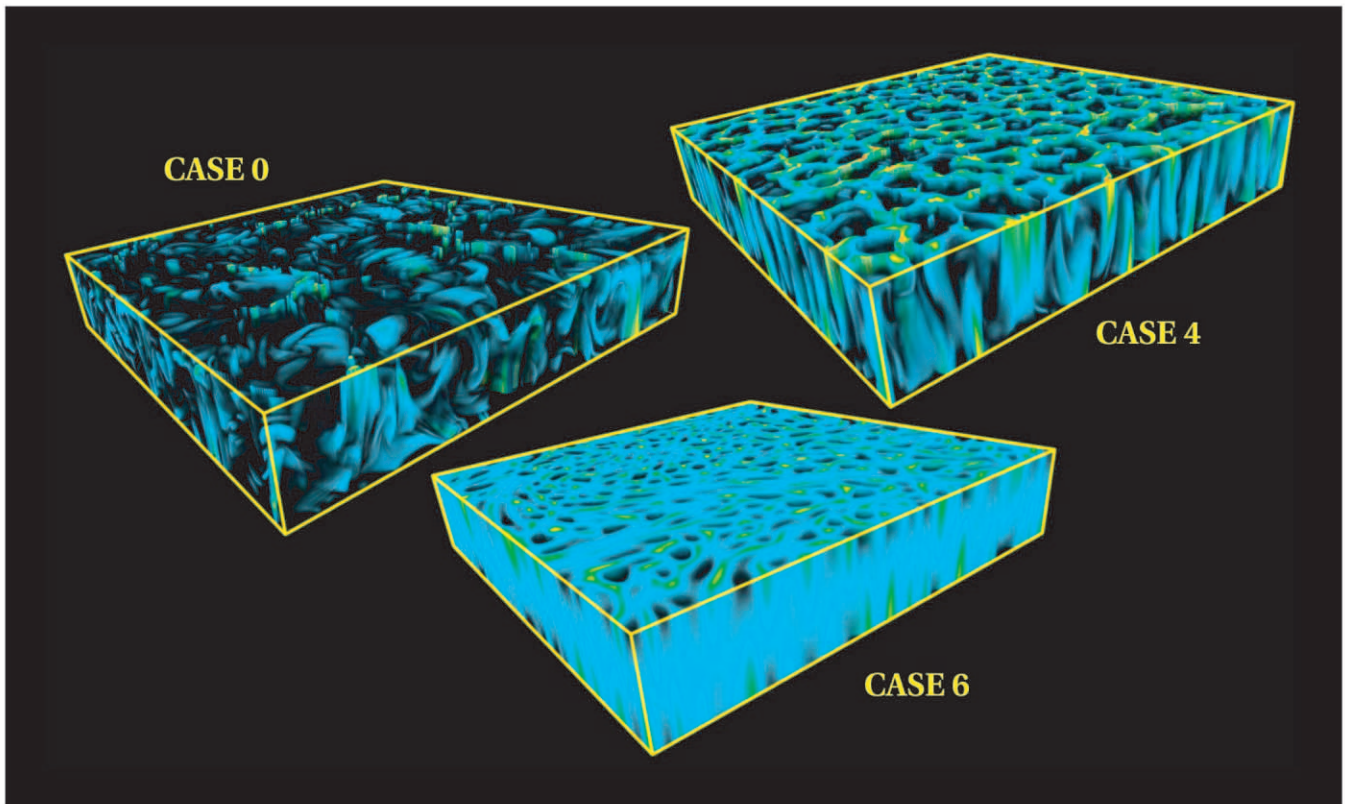


FIG. 1.—Snapshots of magnetic field structures in different regimes. The color volume rendering indicates the field strength $|\mathbf{B}|$ for three cases. Case 0 shows the intermittent structure of the field in a turbulent dynamo with zero imposed magnetic field. Case 4 shows the pattern of cellular magnetoconvection in the intermediate regime, when the imposed field is relatively strong and magnetic flux is swept into a network enclosing plumes as they impinge on the upper boundary. Case 6 is in the oscillatory regime, in which motion is dominated by the magnetic field, but the cellular pattern is distorted by a large-scale two-dimensional circulation. In these images the vertical scale is exaggerated by a factor of 2.

field (Cattaneo 1999). Figure 1 includes a snapshot showing the intermittent structure of the resulting field, which is dominated by the motion. With a strong imposed field, the pattern is quite different. At the top (or bottom) of the layer the field is confined to a continuous network that encloses the convective plumes, also shown in Figure 1. Finally, when the dynamics is dominated by magnetic forces, convection becomes extremely weak, with a pattern that involves both feeble plumes and rolls, again illustrated in Figure 1. A preliminary account of some of these results has appeared elsewhere (Emonet, Cattaneo, & Weiss 2001).

We emphasize that there is no abrupt transition from a turbulent dynamo, when the imposed field is extremely weak, to magnetoconvection, when the field is strong. Rather, there is a gradual change as convection distorts and amplifies the imposed field, until its energy eventually exceeds that of the disordered field generated by dynamo action. The three regimes displayed in Figure 1 are all covered by a single system, with no absolute distinction between dynamos and magnetoconvection.

Our paper is structured as follows. In the next section we formulate the model problem and summarize the relevant linear results; some aspects of the numerical code are described in the Appendix. Then, in § 3, we provide an overview of the nonlinear results, distinguishing between dynamo action and behavior in the strong-field and magnetically dominated regimes. This is followed, in § 4, by

descriptions of the nonlinear solutions. The implications of these results are discussed in § 5.¹

2. FORMULATION OF THE PROBLEM

2.1. The Model System

We consider thermally driven convection in a three-dimensional, Cartesian layer of incompressible (Boussinesq) fluid of depth d , density ρ , kinematic viscosity ν , thermal diffusivity κ , and magnetic diffusivity η . Following standard practice, we adopt the layer depth d , the thermal relaxation time d^2/κ , and the temperature drop across the layer ΔT as the units of length, time, and temperature, respectively. We measure magnetic field intensities in units of the equivalent Alfvén speed $B/(\mu_0\rho)^{1/2}$, where μ_0 is the magnetic permeability of the medium. With these units, and standard notation, the evolution equations read

$$(\partial_t - \sigma\nabla^2)\mathbf{u} + \mathbf{u}\nabla\cdot\mathbf{u} = -\nabla p + \mathbf{J}\times\mathbf{B} + \sigma\text{Ra}\theta\mathbf{e}_3, \quad (1)$$

$$\frac{\partial_t - \sigma}{\sigma_m\nabla^2}\mathbf{B} + \mathbf{u}\cdot\nabla\mathbf{B} = \mathbf{B}\cdot\nabla\mathbf{u}, \quad (2)$$

$$(\partial_t - \nabla^2)\theta + \mathbf{u}\cdot\nabla\theta = u_3, \quad (3)$$

$$\nabla\cdot\mathbf{B} = \nabla\cdot\mathbf{u} = 0, \quad (4)$$

¹ Qualitative behavior of the solutions is best appreciated by inspecting the MPEG animations available at <http://flash.uchicago.edu/~mhd>.

where $\mathbf{J} = \nabla \times \mathbf{B}$ is the current density and θ denotes the temperature fluctuations relative to a linear background profile (see, e.g., Chandrasekhar 1961). Three dimensionless numbers appear explicitly: the Rayleigh number $\text{Ra} = g\alpha\beta d^4 / \kappa\nu$ (where g is the gravitational acceleration, α is the coefficient of thermal expansion, and β is the superadiabatic temperature gradient), which measures the strength of thermal buoyancy relative to dissipation, and the kinetic and magnetic Prandtl numbers,

$$\sigma = \frac{\nu}{\kappa} \quad \text{and} \quad \sigma_m = \frac{\nu}{\eta}. \quad (5)$$

We consider both cases in which a vertical magnetic field $B_0 e_3$ is externally imposed and cases in which the magnetic field is due solely to dynamo action. For this reason, we choose not to measure the magnetic field intensity in units of B_0 , as is common practice in magnetoconvection studies, and as a result the Chandrasekhar number Q does not appear explicitly in front of the Lorentz force term in equation (1). However, because of the usefulness of the Chandrasekhar number as a dimensionless measure of the Lorentz force relative to dissipative effects, in those cases in which it can be meaningfully defined, we note that it can be expressed as

$$Q = \frac{B_0^2 \sigma_m}{\sigma^2}. \quad (6)$$

For similar reasons, we note that the ratio of the magnetic to the thermal diffusivity (the magnetic Schmidt number), also used in a number of studies of magnetoconvection, is given by

$$\zeta = \frac{\eta}{\kappa} = \frac{\sigma}{\sigma_m}. \quad (7)$$

For computational convenience, we consider idealized (or “illustrative”) boundary conditions such that the temperature fluctuations, the normal component of the velocity, the tangential component of the stress tensor, and the horizontal component of the magnetic field vanish on the upper and lower boundaries. These formally correspond to

$$\theta = u_3 = \partial_z u_1 = \partial_z u_2 = B_1 = B_2 = 0 \quad \text{at} \quad z = 0, 1. \quad (8)$$

In the horizontal directions we assume that all fields are periodic with periodicity λ . It follows that the net magnetic flux across the upper or lower boundary of the box is conserved.

Our primary motivation is to provide a systematic study of the interaction of convection with magnetic fields in the strongly nonlinear regime. This, in turn, imposes certain requirements on the choice of defining parameters. Near the onset of convection, in the absence of a magnetic field, the typical diameter of a (periodic) convective cell is approximately 3 times the layer depth, this value increasing somewhat as convection becomes more supercritical. Thus, in order to allow for the natural development of convective structures without undue effects from the horizontal boundary conditions, the horizontal periodicity must be sufficiently large. Similarly, we recall that the critical Rayleigh number, Ra_0 , for the onset of convection, in the absence of external magnetic fields and with our choice of boundary conditions, is given by $\text{Ra}_0 = 27\pi^4/4 \approx 657.51$ (Chandrasekhar 1961). Thus, in order to develop a vigorous state of convection the Rayleigh number must be

much greater than this critical value. Previous experience with similar types of calculations leads us to choose $\lambda = 10$ and $\text{Ra} = 5 \times 10^5$ as reasonable compromises between physical requirements and computational feasibility. Similar considerations have contributed to our choice of Prandtl numbers. The case in which all Prandtl numbers are unity is particularly favorable from the numerical point of view, for then all boundary layers have roughly the same thickness and a given computational grid resolves all the field variables equally. On the other hand, in the present case we want to emphasize magnetic effects, and thus we have chosen $\sigma = 1$ and $\sigma_m = 5$ ($\zeta = 0.2$) so that the magnetic Reynolds number $\text{Rm} = \sigma_m U / \sigma$ (where U is a typical dimensionless velocity) is 5 times higher than the ordinary Reynolds number.

We solve equations (1)–(4) numerically by standard pseudospectral methods optimized for machines with parallel architecture. Details concerning the numerical methods as well as resolution and performance considerations are presented in the Appendix. Note that we are only able to take advantage of this rapid pseudospectral technique because we have adopted the Boussinesq approximation with idealized boundary conditions. Even so, a typical run requires 60–100 CPU hours on a 128 processor Cray T3e.

2.2. Linear Analysis

Although we are mostly interested in the nonlinear regime, we recall in this section some elementary results from the linear theory of magnetoconvection, which we specialize for our choice of parameters and boundary conditions. These are used primarily to set the stage for the nonlinear calculations and to give us some idea of where we are in parameter space.

In the absence of magnetic fields the growth rate of infinitesimal perturbations to the conductive solution is determined by a quadratic dispersion relation. Convection sets in as a direct instability, i.e., an overturning convection, at the critical Rayleigh number Ra_0 and with a critical horizontal wavenumber of $\pi/\sqrt{2}$. The presence of an external magnetic field adds further complexity to the problem and allows for the possibility of overstability, i.e., instability to growing oscillations (Chandrasekhar 1961; Proctor & Weiss 1982).

If $\sigma/\sigma_m = \zeta \geq 1$, convection sets in as a direct instability for all values of the magnetic field strength; if, on the other hand, $\sigma/\sigma_m < 1$, as is the case here ($\sigma/\sigma_m = 0.2$), convection sets in as a direct instability if the imposed field is below a critical value and as an oscillatory instability if it is above it. This critical value depends on the horizontal scale of the perturbations and, in terms of the Chandrasekhar number, can be written as

$$Q_{\text{crit}} = \frac{k^4}{\pi^2} \frac{1 + \sigma}{\sigma_m - \sigma}, \quad (9)$$

where k_h and k are the horizontal and total wavenumbers, respectively: $k_h^2 = k_x^2 + k_y^2$ and $k^2 = k_h^2 + \pi^2$. Since we work at a fixed value of the Rayleigh number, it is convenient to obtain the critical values of Q , and hence B_0 , at which stationary and oscillatory bifurcations occur. There is a stationary bifurcation at

$$Q^{(e)} = \frac{k_h^2 \text{Ra} - k^6}{\pi^2 k^2}. \quad (10)$$

There is also an oscillatory bifurcation at

$$Q^{(o)} = \frac{\sigma_m}{\sigma^2} B_0^{(rmo)2} = \frac{(1 + \sigma)}{\pi^2 \sigma^2} \left[\frac{\sigma_m^2 k_h^2 \text{Ra}}{(1 + \sigma_m) k^2} - (\sigma + \sigma_m) k^4 \right], \quad (11)$$

provided that

$$\frac{(k_h^2 + \pi^2)^3}{k_h^2} < \frac{(\sigma_m - \sigma)}{(1 + \sigma_m)} \text{Ra}. \quad (12)$$

The corresponding critical curves for $\text{Ra} = 500,000$, expressed in terms of B_0 , are shown in Figure 2. It is apparent that for moderate values of k_h , convection sets in at an oscillatory bifurcation and that no unstable linear mode exists for $B_0 > 272$. The dotted horizontal lines correspond to the values of B_0 used in our calculations.

An important aspect of linear theory is that it may be used to predict a definite relationship between the horizontal scale of the unstable modes and the strength of the imposed field. Figure 2 shows that, for most values of B_0 for which the system is linearly unstable, the instability extends to a broad band of horizontal wavenumbers, giving little indication as to the preferred horizontal scale of convection as B_0 is varied. A more revealing picture is obtained by looking at the variations of the critical values of the Rayleigh number as a function of the horizontal wavenumber for different values of B_0 , which are shown in Figure 3. Each curve has a single minimum corresponding to the most unstable wavenumber. A definite trend becomes apparent indicating that, at least in linear theory, the preferred horizontal scale of convection *decreases* with increasing field strength; i.e., for stronger fields, narrower convective cells are more easily destabilized. The results of our calculations are, of course, nonlinear and, in general, not close to the curves of marginal stability, except possibly for the cases with very large B_0 . Nevertheless, as we shall see, a similar trend is observed.

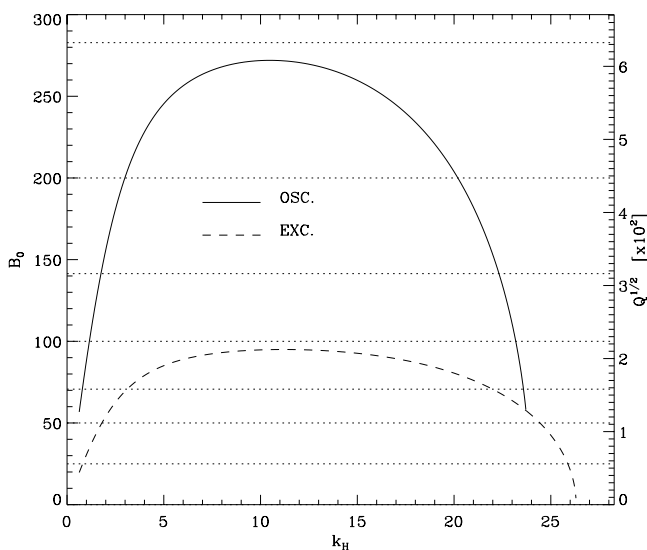


FIG. 2.—Linear theory: the oscillatory and stationary bifurcations. The solid and dashed lines show $B_0^{(e)}$ and $B_0^{(rmo)}$, respectively, as functions of the horizontal wavenumber k_h . The right-hand ordinate axis shows the corresponding values of $Q^{1/2}$, while the horizontal dotted lines indicate the values of B_0 for cases 1–7.

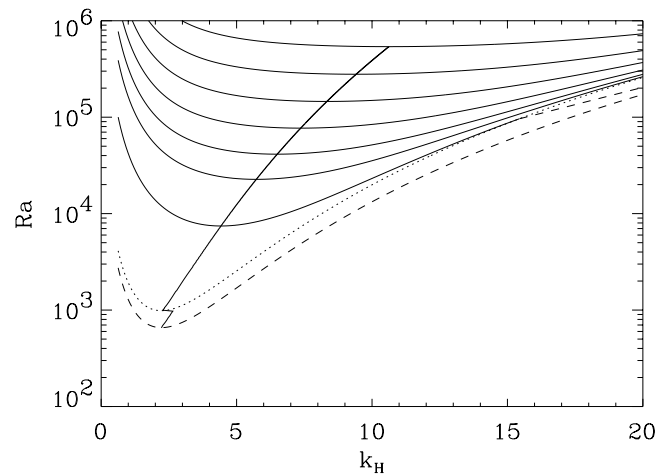


FIG. 3.—Critical Rayleigh numbers for the onset of convection, as functions of the horizontal wavenumber k_h , for increasing values of B_0 , corresponding to different cases in our simulations. The dashed line is the zero field case, and the dotted line corresponds to the transition between direct and oscillatory behavior. The minima for each curve are joined by a solid line, indicating the trend toward higher wavenumbers and narrower cells as the imposed field is increased.

3. FROM DYNAMO ACTION TO MAGNETOCONVECTION

We first list all our simulations and present an overview of the results.

Table 1 outlines the eight simulations that form the basis for the present work. Case U is a purely hydrodynamic simulation used as both a reference and the initial condition for all the other simulations. The setups for cases 0–7 differ only in the magnitude of the externally imposed magnetic field B_0 . In the dynamo case 0, there is no uniform field ($B_0 = 0$), but a weak seed field with no net vertical flux was introduced. In each case, there is an initial phase, lasting a few turnover times, in which the magnetic energy grows to its eventual stationary value. In the dynamo case, the *nonlinear* part of the saturation process is somewhat longer and proceeds over approximately 20 turnover times. Once a (statistically) stationary state was reached, the simulations were

TABLE 1
PARAMETER SPACE

Case	B_0	Re	Rm	E_m/E_k
U	245
0 ^a	Seed	201	1005	0.20
1.....	25	143	715	0.95
2.....	50	114	571	1.69
3.....	$50\sqrt{2}$	100	499	2.33
4.....	100	85	425	3.48
5.....	$100\sqrt{2}$	75	373	5.67
6.....	200	59	296	12.76
7.....	$200\sqrt{2}$	41	205	47.76

NOTE.—The following parameters are the same for all the cases: aspect ratio $10 \times 10 \times 1$, $\text{Ra} = 500,000$, $\sigma = 1$, $\sigma_m = 5$, and a numerical resolution of $512 \times 512 \times 97$ Fourier collocation points. At time zero, $E_{k0} = 30,000$, and the rms velocity is $u_0 = 245$.

^a From Cattaneo 1999.

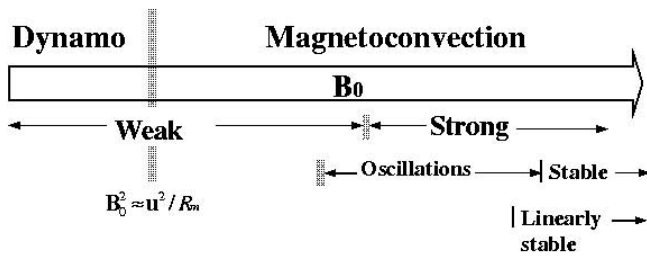


FIG. 4.—Schematic representation of the different regimes obtained as the value of the net magnetic flux through the box is increased. Thick solid lines denote hard transitions, while fuzzy lines indicate more gradual transitions.

continued for between 50 and 100 turnover times. All average quantities were computed by sampling over the stationary part of the simulations.

It is apparent in Table 1 that, as B_0 increases, the resulting (magneto-) convection settles down to different regimes characterized by an increasing ratio of the average magnetic to kinetic energy densities. This increase is also manifest as changes in dynamical behavior. The purpose of this section is to provide some overall organization and to identify the various regimes that characterize the solutions. These are mostly expressed in terms of different qualitative behaviors. More quantitative assessments of the properties of the solutions are presented later. The basis for the present discussion is the schematic diagram in Figure 4, which shows the various regimes in terms of the strength of the imposed magnetic field. Moving horizontally from left to right corresponds to increasing the imposed field strength. On the extreme left are cases in which the imposed field is zero and on the extreme right, cases in which the imposed field is strong enough to suppress convection altogether. Transitions from one behavior to another are indicated by vertical lines, with the convention that thick solid lines indicate hard transitions, i.e., ones that occur at a precise value of B_0 , and thick gray lines correspond to more gradual transitions that occur over a range of values.

The first, and possibly the most important, transition is between the dynamo regime and the magnetocovection regime. The distinction is a conceptual one that can best be understood in terms of the contributions to the magnetic energy on small scales. There are two distinct mechanisms that can amplify the magnetic energy at scales small compared to the velocity correlation length: one is a process of cascade from large to small scales. Physically, it corresponds to the tangling up of the large-scale component of the magnetic field by the fluid motions. The other is the dynamo instability itself, which can generate magnetic energy directly at scales comparable with or smaller than that of the velocity. If the large-scale field is extremely weak (kinematic), there is a linear relationship between the energy of the large-scale field and the (magnetic) energy at small scales. The coefficient of proportionality depends on the magnetic Reynolds number and the specific geometry of the magnetic structures at small scales, i.e., sheets, tubes, etc. The dynamo contribution, on the other hand, depends solely on the nonlinear properties of the dynamo saturation process and is typically related to the kinetic energy of the flow—the equipartition energy. Thus, the relative importance of the two energetic contributions depends on the strength of the imposed field. We identify the dynamo

regime with those cases in which most of the small-scale (magnetic) energy is generated by dynamo action and the magnetocovection regime with those cases in which most of the small-scale energy is due to the cascade process. The transition between the two regimes occurs when the two contributions are comparable. We note that because of the absence of rotation, or of any other mechanism capable of breaking reflectional symmetry in the present case, we can rule out the possibility of inverse cascades.

The second distinction is between the weak magnetic regime and the strong magnetic regime. Broadly speaking, in the weak-field regime the convection remains sufficiently vigorous to concentrate the magnetic field into intense, isolated structures; in the strong-field regime magnetic tension forces reduce the amplitude of the convection to a point that magnetic field concentration is no longer possible and the magnetic field fills all available space. The distinction here is best expressed in terms of magnetic field morphology and can be made quite precise by looking at the probability distribution function for magnetic fluctuations at the surface of the layer. As we shall see in more detail presently, in the weak-field regime the horizontal flows near the upper boundary are sufficiently powerful to sweep the magnetic field into the cellular lanes and corners, leaving large areas devoid of strong fields. In this regime the most probable value for the magnetic field intensity at the surface is zero; i.e., because of flux concentration, most of the surface area is covered by weak magnetic fluctuations of either polarity. In the strong-field regime, flux concentration is suppressed, and the most probable value for the magnetic field intensity at the upper surface is close to the mean-field value.

We also distinguish between an oscillatory and a non-oscillatory regime. For sufficiently strong values of the mean field, but still in the weak-field regime, the volume-averaged kinetic and magnetic energies begin to display an oscillatory behavior with a definite frequency and long time phase coherence. The ratio of the amplitude of the oscillations (in kinetic energy) to the value of the corresponding time average increases with increasing mean field strength. This trend appears to persist until the convection is completely suppressed.

Finally, we note that convection is possible for values of B_0 that are slightly higher than the critical one for linear stability. This is not surprising, and the tendency for magnetocovection to be subcritically unstable is well documented (see, e.g., Proctor & Weiss 1982).

4. PROPERTIES OF THE NONLINEAR SOLUTIONS

4.1. Surface Features

The differences between the various regimes appear most strikingly in gray-scale plots of the temperature fluctuations, θ , and of the vertical magnetic field, B_z , in a horizontal plane close to the surface. The dynamo case is shown in Figure 5, whereas the magnetococonvective cases 1–6 are plotted in Figures 6 and 7. The temperature plots reveal the structure of the velocity flow, with light shades corresponding to (hot) rising plasma and dark shades indicating the location of (cold) downdrafts. The surface plots of B_z provide the corresponding spatial distribution of the magnetic field, with white and black indicating upward and downward orientations, respectively.

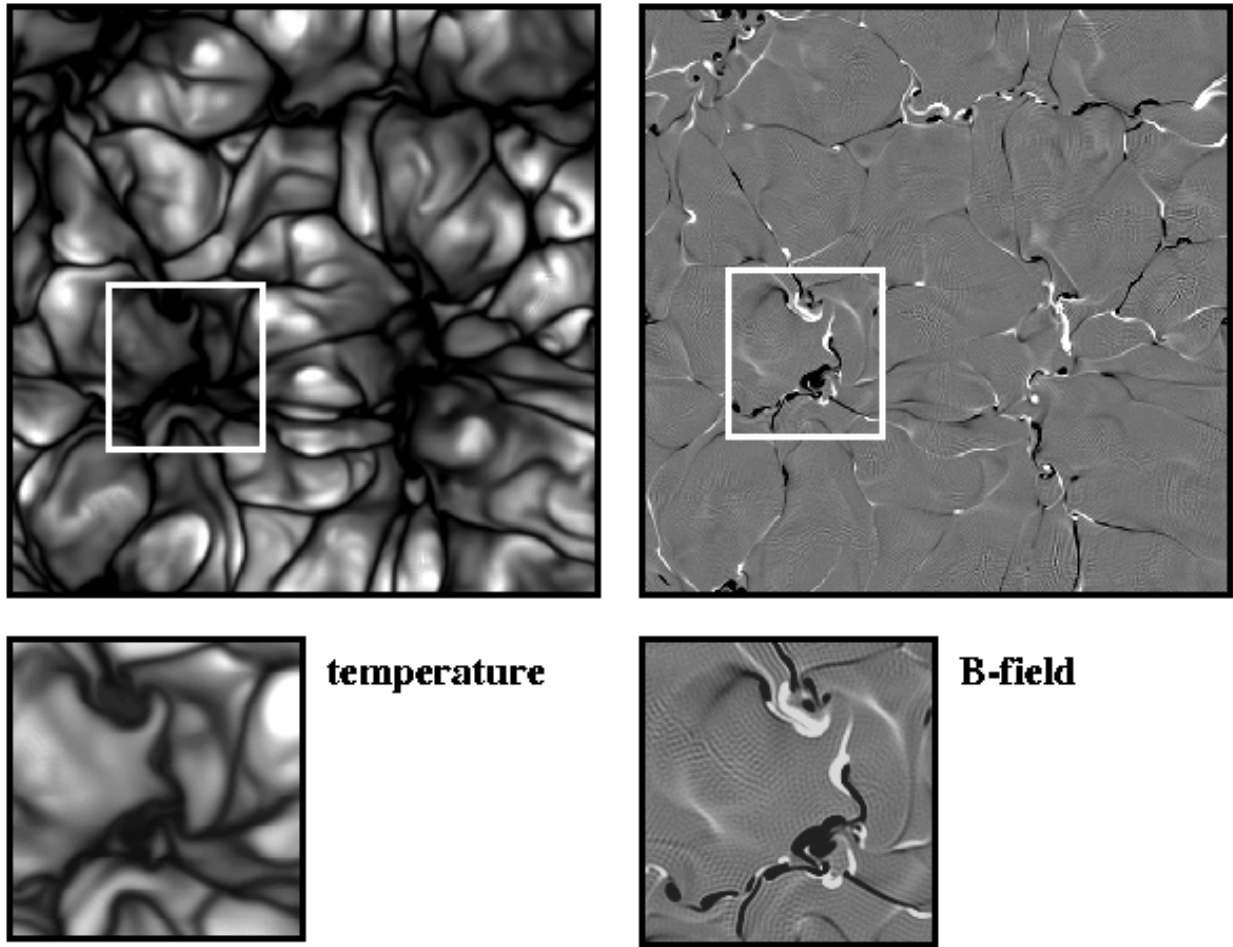


FIG. 5.—Gray-scale plots of surface temperature and magnetic fluctuations for the dynamo solution (case 0). The insets show details of behavior near the swirling vortex at a corner in the mesocellular network. In the left-hand panels light (dark) regions denote warmer (cooler) temperatures just below the upper boundary. In the right-hand panels light (dark) patches correspond to upward- (downward-) directed magnetic fields, while gray regions are nearly field-free. Note that fields of both signs are present near the vortex.

In the dynamo solution (Fig. 5) the system is dominated by the turbulent flow, and as a consequence the magnetic field is concentrated on the borders of the convection cells. Interestingly, the largest magnetic fluctuations are not located around the granules but rather on the corners of a broader mesocellular pattern, very similar to the mesogranulation observed in the solar photosphere—see Cattaneo et al. (2001) for a detailed account of these large cells. These corners are the locations of the strongest downdrafts. The magnetic field in these regions does *not* exhibit a monolithic structure. Instead, it is the complicated outcome of the continuous inflow of magnetic elements with different polarities by the swirling converging motions.

When the run is started by adding a very weak uniform field instead of a random seed field (case 1, in which the magnetic energy of the initial field is only 1% of the kinetic energy in the unmagnetized case U), the system settles into a magnetoconvective regime that is very close to the dynamo state. Indeed, the surface distributions of θ and B_z (upper left-hand panels in Figs. 6 and 7) are very similar in cases 1 and 0. The main difference resides in the fact that in case 1 the polarity is mostly positive.

For higher values of B_0 the convective pattern is affected by the magnetic field, as the Lorentz force becomes increasingly effective in preventing overturning motions. As a result, the horizontal scale of convection decreases. This is clearly visible in Figures 6 and 7, where from the top left to the bottom right the imposed vertical magnetic flux is increased by factors of $\sqrt{2}$. This feature is reminiscent of abnormal granulation in the solar photosphere (Title et al. 1992). Another change in the surface features is the rapid disappearance of the mesocellular structures as B_0 is increased (compare cases 1, 2, and 3 in Figs. 6 and 7). By the time B_0 is equal to 100 (case 4) only one scale of convection is left for both θ and B_z .

The transition from the weak to the strong magnetic regime occurs somewhere between cases 5 and 6. Whereas θ and B_z are still displaying a cellular pattern in case 5, this ceases to be true in case 6. Some large-scale structures, which cross the entire domain, have appeared. Clearly, the magnetic field dominates the system, and the flow is no longer able to concentrate the magnetic flux on the border of convective cells. In fact, no convective cells are left.

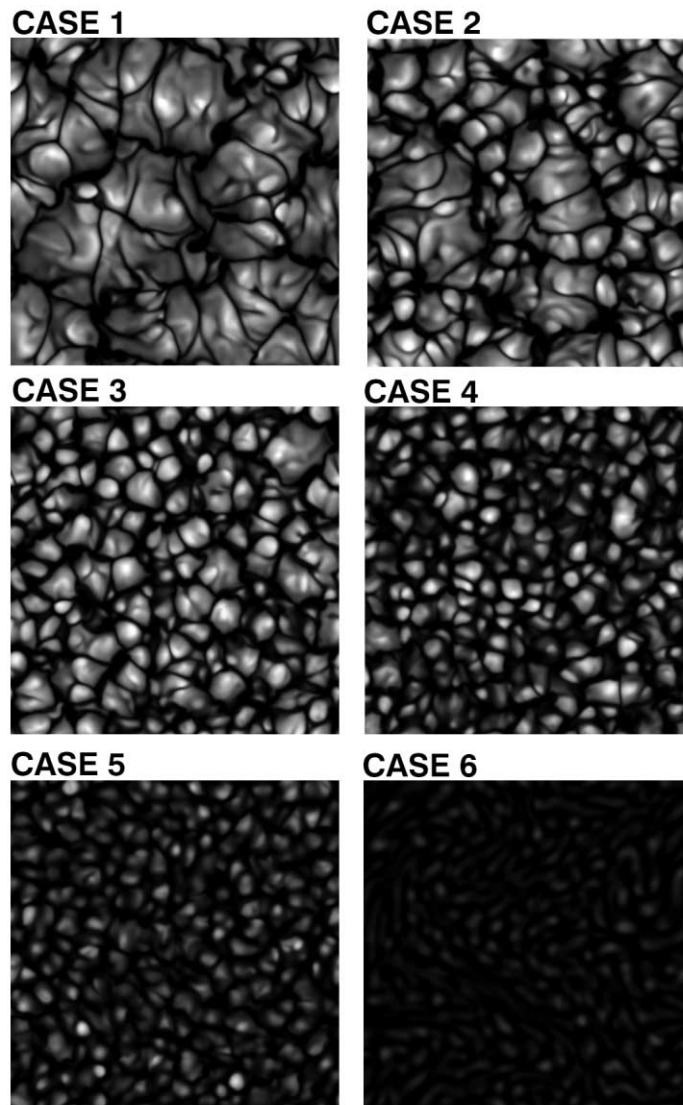


FIG. 6.—Snapshots showing temperature fluctuations near the upper surface for cases 1–6. The scaling is the same for each case. As B_0 is increased, the cells grow narrower and convection becomes feebler, so that the range of variation in the temperature diminishes.

A more quantitative representation of these results can be obtained by computing horizontal power spectra of the temperature and the magnetic field. For small values of B_0 , these spectra are bimodal, with two peaks that correspond to the cellular and mesocellular scales. For larger values of B_0 , these peaks merge, and the patterns are characterized by a single cell size. Figure 8 summarizes this effect. As expected, the scale of the cellular pattern decreases as B_0 is increased. A similar trend is also observed in linear theory. What is of some interest is that it is the curve of marginal stability that best captures the trend (see Fig. 3) and not, for instance, the curve of maximum growth rate. A plausible, simple interpretation of this result is that in some average sense, the nonlinear terms renormalize the transport and diffusivities so as to keep the system near marginal stability.

4.2. Kinetic and Magnetic Energies

The magnetic and kinetic energies of the system also reflect the transitions from one regime to the other. This is illustrated in Figure 9, in which the time evolution of the

volume-averaged quantities $\langle B^2 \rangle$ and $\langle u^2 \rangle$ are plotted for cases 0, 1, 4, and 6. The asymptotic values for all the cases are shown in Figure 10.

In case 0, the initial seed field is amplified by dynamo action. The increase in $\langle B^2 \rangle$ occurs in three stages (Cattaneo 1999): first, a kinematic phase (up to $t = 0.06$) in which the magnetic energy increases exponentially, then a phase ($0.06 \leq t \leq 0.12$) in which nonlinear effects have become important while $\langle B^2 \rangle$ increases linearly with time, and finally, a saturation phase ($0.12 \leq t \leq 0.16$) in which the growth of the magnetic energy progressively declines. The magnetic energy eventually settles down to a statistically steady state, with $\langle B^2 \rangle \approx 0.2 \langle u^2 \rangle$, while the kinetic energy has decreased to two-thirds of its original value in the field-free case. These values are independent of the strength and form of the initial seed field.

If there is an initial mean field, however, then the asymptotic value of $\langle B^2 \rangle$ is a monotonically increasing function of B_0 . In the *dynamo regime*, where B_0 is extremely small, the final value of $\langle B^2 \rangle$ is barely affected and remains close to its value in case 0. In all the cases 1–7, the imposed field is

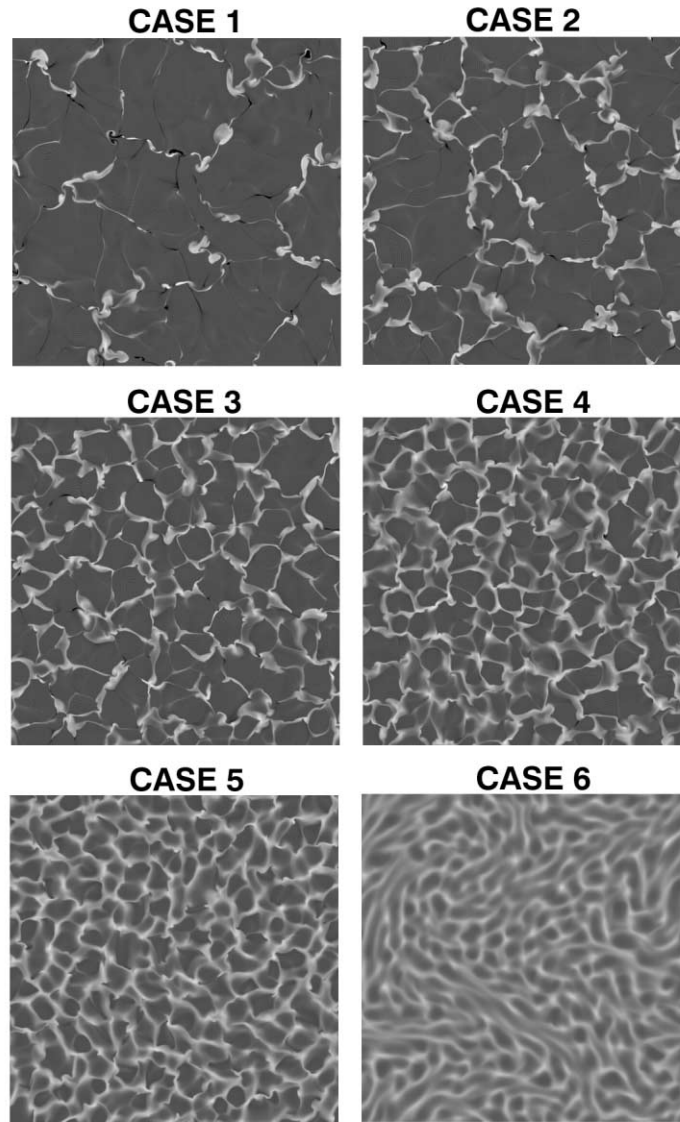


FIG. 7.—Same as Fig. 6, but showing the surface magnetic field. In these gray-scale plots dark and light regions again denote oppositely directed fields, and the scaling is the same for all cases. Note that fields with both directions are present in case 1, but the imposed field direction predominates as B_0 is increased. The mesocellular pattern persists in the convective regime (cases 1 and 2), but only smaller cells are present in the intermediate regime (cases 3–5). Case 6 is in the oscillatory regime.

strong enough to have a significant effect on the flow. It is helpful to distinguish between three different regimes, depending on the relative strengths of the convective and Alfvénic responses. In the *convective regime* (cases 1 and 2) the mesocellular pattern is clearly visible, and the approach to the final state is virtually monotonic, without any significant oscillations. As B_0 increases, $\langle B^2 \rangle$ also increases, while $\langle u^2 \rangle$ decreases, and they eventually swap around. In the *intermediate regime* (cases 3–5) the magnetic energy is greater than the kinetic energy, the Alfvénic response is stronger, and the mesocells disappear, while the approach to the final state has a strong oscillatory component. The final kinetic energy remains time-dependent without being oscillatory. Cases 6 and 7 are in the *oscillatory regime*: the approach to the asymptotic state has a strong oscillatory component, and coherent oscillations persist indefinitely at later times. The magnetic field everywhere is almost uniform, and, as can be seen from Figure 10, the energy of the

fluctuating field is comparable to the kinetic energy and small compared to the energy of the mean field, i.e.,

$$\langle u^2 \rangle \approx \langle B^2 \rangle - B_0^2 \ll \langle B^2 \rangle. \quad (13)$$

It follows that the oscillatory regime corresponds to an ensemble of trapped Alfvén waves; as expected, the frequency is very close to the Alfvén speed B_0 .

The magnetic pattern for case 6, in Figure 7, shows both linear and cellular features. At first sight, this seems to indicate a competition between convective rolls and cells, but that is not what happens. The elongations are, in fact, the manifestations of a large-scale circulation pattern whose effect is to deform and elongate the cells. This circulation is purely horizontal and is independent of depth. Figure 11 shows the variation of kinetic energy of the horizontal motion, $\langle u_x^2 + u_y^2 \rangle$, with B_0^2 for cases 1–7. Also shown are the corresponding energies for the large-scale components

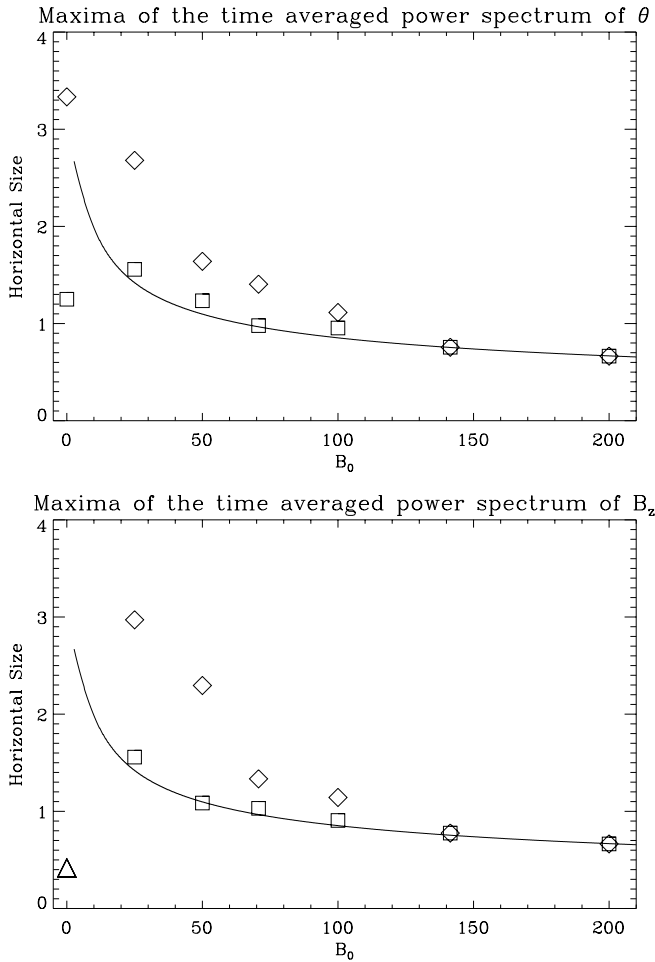


FIG. 8.—Typical horizontal sizes of the temperature and magnetic fluctuations near the surface as functions of B_0 . The squares and diamonds correspond to the maxima of the time-averaged power spectra of θ and B_z in a horizontal plane near the top of the computational box. The solid line represents the prediction from linear theory as represented in Fig. 3. The diamonds are the signature of the mesocellular pattern, whereas the squares show the smaller cellular pattern. Notice that in case 0 (the dynamo) the magnetic field displays only one preferred scale, namely, the size of the magnetic concentrations at the corners of the mesocells, which is represented by a triangle. The other scales, corresponding to cells and mesocells, are clearly visible in Fig. 5, but they do not appear here because their power is small in comparison to the power stored in the smaller intercellular scale.

of the flow, with horizontal wavenumbers $k_h \leq 3$, first for all vertical wavenumbers k_z and then only for the z -independent part ($k_z = 0$). The coalescence of the two latter sets of values by case 3 once again indicates the disappearance of mesocells in the intermediate regime. For cases 3–7, all the large-scale horizontal flow is depth-independent. Although there is much more energy in the cellular motion than in the large-scale flow for cases 3–5, all the horizontal energy is in the large-scale circulation for cases 6 and 7. We conjecture that the dominant magnetic field confers so much rigidity to the slender small-scale structures that the whole system behaves like two-dimensional turbulence, with an inverse cascade that drives a large-scale flow.

Finally, we may note that the oscillatory bifurcation (at $B_0 = 272$; see Fig. 2) is severely subcritical. Although $\langle u^2 \rangle \ll \langle B^2 \rangle$ for case 7 (with $B_0 = 283$), both the Reynolds number and the magnetic Reynolds number are large, as can be seen from Table 1.

4.3. Probability Distribution Functions

In this subsection we analyze three of the solutions in more detail, namely, the dynamo run (case 0), one solution in the intermediate regime (case 4), and one in the oscillatory regime (case 6). In each case the system organizes the fields into different spatial structures, and insights into these patterns can be obtained by constructing the probability distribution functions (PDFs) of, say, the vertical component of the magnetic field or, in other words, the probability of finding a fluid parcel with magnetic field B_z in an interval of width dB_z about the value B_z . PDFs for the velocity can similarly be defined. The PDFs of the (vertical) magnetic field in two horizontal planes, one at the top, the other in the middle of the layer, are plotted in Figure 12.

In cases 0 and 4, the maxima in the PDFs are located at or near zero intensities. Thus, most of the volume is filled with weak magnetic fields. Indeed, if, for example, we integrate the PDF over $|B_z| \leq u_{\text{rms}}$ in the upper layers of the dynamo case, we find that subequipartition fields have a filling factor of 97%. This agrees with recent measurements of weak fields in the solar photosphere (see Stenflo 1999 and references therein). The fact that most of the volume is filled with weak magnetic field indicates that, for these cases, the turbulent flows are vigorous enough to concentrate the magnetic flux into thin isolated structures. This concentration process becomes more difficult to achieve as the mean magnetic flux through the box is increased. In case 4, for instance, the additional flux creates a hump on the right-hand side of the PDF. However, the convection is still able to concentrate the magnetic field at the border of the cells. In the strongly magnetic case, the vigor of convection is reduced to such an extent that the flows can no longer confine the magnetic field, and the latter permeates most of the volume. The corresponding PDFs peak at a value slightly less than that of the mean and become supported on the positive side only; i.e., the magnetic field has positive (up) polarity everywhere.

When the mean field is zero or *very* small the PDFs are symmetric or nearly symmetric about $B_z = 0$, displaying a (stretched) exponential shape up to values comparable to the equipartition strength (Cattaneo 1999). This shows that the relative amounts of very strong and very weak magnetic fluctuations are higher than if the magnetic distribution was the simple result of random processes (Gaussian distribution). In these cases, the system produces a magnetic field with two main components: strong magnetic fluctuations located near the strongest downdrafts (with small filling factors) and weak magnetic fields that are found everywhere else (see also § 4.1). If a noticeable amount of mean magnetic flux is added to the system, but such that it remains in the weak-field regime, the shape of the PDF is modified, and an additional hump appears on the right-hand side. Its Gaussian shape suggests that the process of magnetic intensification of the imposed magnetic field is different from the generation of magnetic fluctuations by dynamo action.

In contrast with the PDFs for the magnetic fluctuations, the PDFs for the velocity fluctuations in the top and middle layers show a Gaussian behavior in all the cases (Fig. 13). The main differences from one case to the other are the narrowing of the distribution and the displacement of the maxima toward smaller velocities. These differences mainly reflect the decrease of the amount of kinetic energy in the system as B_0 is increased.

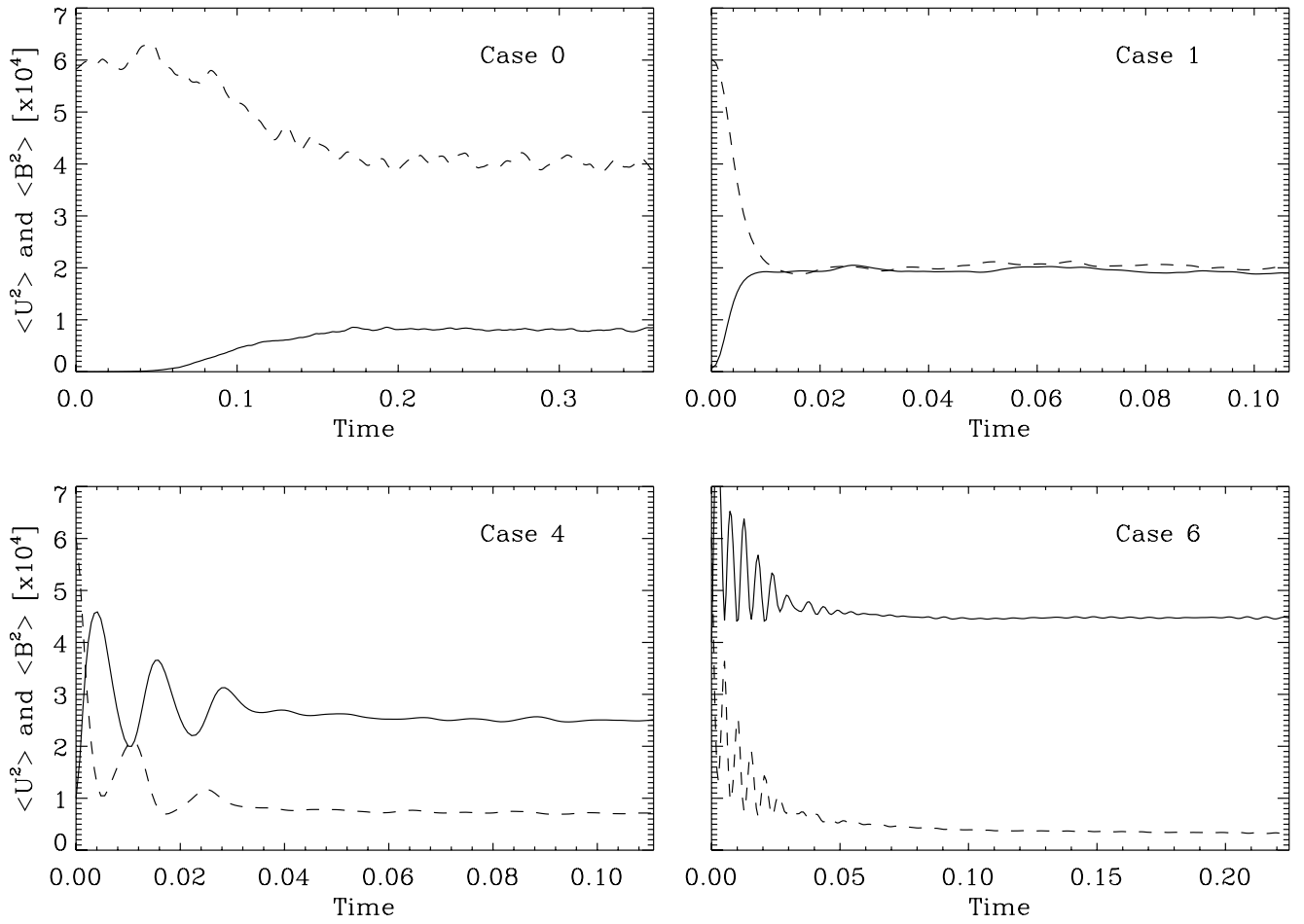


FIG. 9.—Time evolution of the magnetic and kinetic energy densities for the cases 0, 1, 4, and 6. In the dynamo regime (case 0) the kinetic energy is 5 times greater than the magnetic energy. For case 1, in the convective regime, the energies are nearly equal. In the intermediate regime (case 4) the magnetic energy is greater and there are strong transient oscillations. Small amplitude oscillations persist indefinitely in case 6.

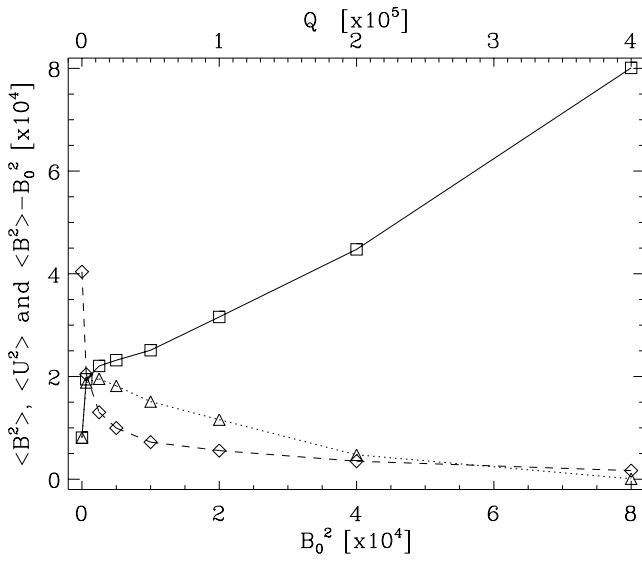


FIG. 10.—Asymptotic values of the mean magnetic and kinetic energy densities for all the runs. The squares, connected by a solid line, show the total magnetic energy density, while the diamonds, connected by a dashed line, show the kinetic energy density. The triangles, connected by a dotted line, indicate the difference between the mean magnetic energy and the energy of the relevant uniform field; for case 0, all the energy is in the fluctuating fields, while for case 7, nearly all the energy is in the mean imposed field.

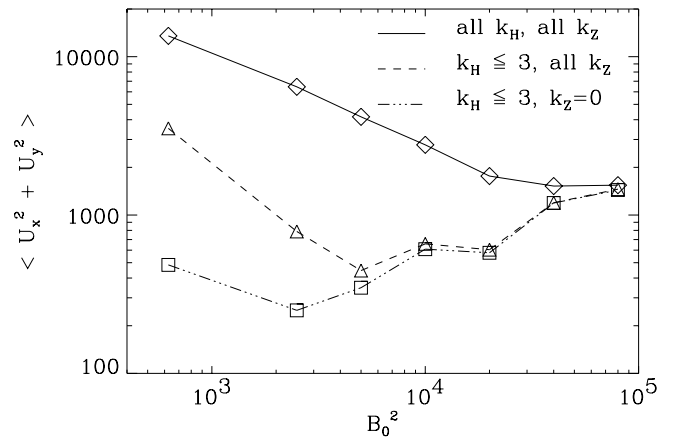


FIG. 11.—Kinetic energy of the horizontal motion as a function of B_0^2 for cases 1–7. The diamonds, connected by a solid line, show the combined energy of all Fourier modes. The triangles, connected by a dashed line, show only those modes with a horizontal wavenumber $k_H \leq 3$, while the squares, connected by a triple-dot-dashed line, show only those modes with $k_H \leq 3$ that do not vary in the vertical z -direction. For cases 3–7, the large-scale flow is two-dimensional and independent of z .

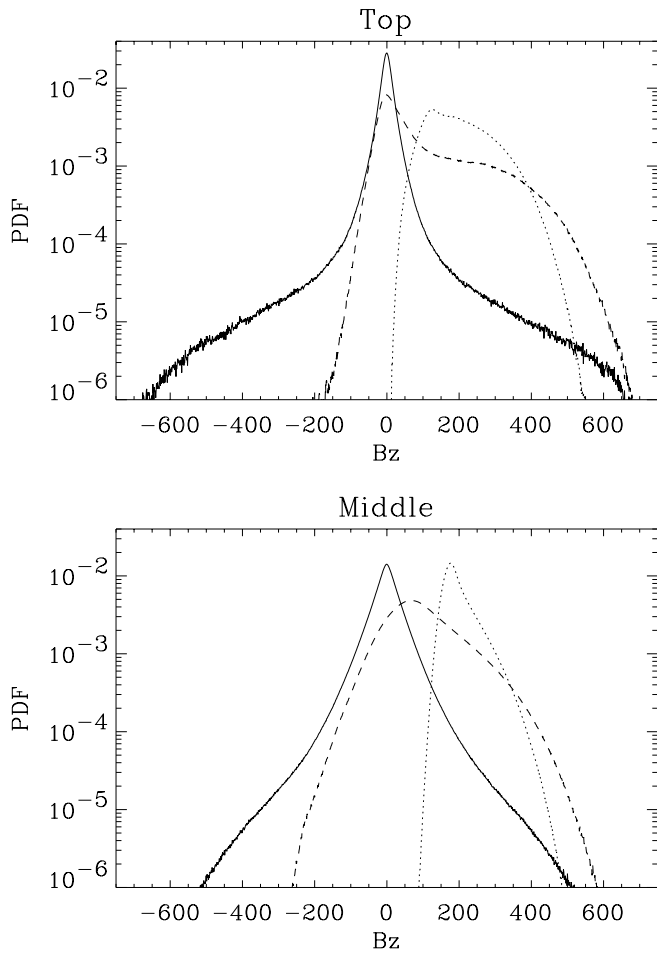


FIG. 12.—PDFs of the signed magnetic field, $|\mathbf{B}| \times \text{sgn } B_z$. The top panel shows values near the top of the computational box (upper thermal boundary layer), while the bottom panel shows values in the middle of the box ($0.24 < z < 0.76$). The solid line corresponds to the dynamo solution (case 0), the dashed line shows case 4, in the intermediate regime, and the dotted line shows case 6, in the oscillatory regime. Note the shift from a profile that is symmetric about zero to one with positive values only.

Finally, there are also some differences between the PDFs computed in the surface layers and those measured around the middle horizontal plane. Because of the presence of the impenetrable upper boundary, the PDFs for the magnetic fluctuations become stretched exponentials near the upper boundary, where the magnetic field becomes strongly intermittent. Thelen & Cattaneo (2000) have studied the influence of several different boundary conditions on the PDFs. They found that near the surface the shape of the PDFs for the magnetic field is affected by the choice of boundary condition. In the interior, however, the PDFs are similar for all boundary conditions, remaining close to an exponential. The PDFs for the velocity fluctuations show fewer differences between middle and top. The main distinction is the higher value of the most probable speed in the top layers.

4.4. Up-Down Symmetry

Boussinesq systems, or more generally, systems with weak stratification, display an up-down symmetry that is not present in more strongly stratified layers. This symmetry has some important consequences for the geometry of the resulting flows. The pattern of convective cells at the upper

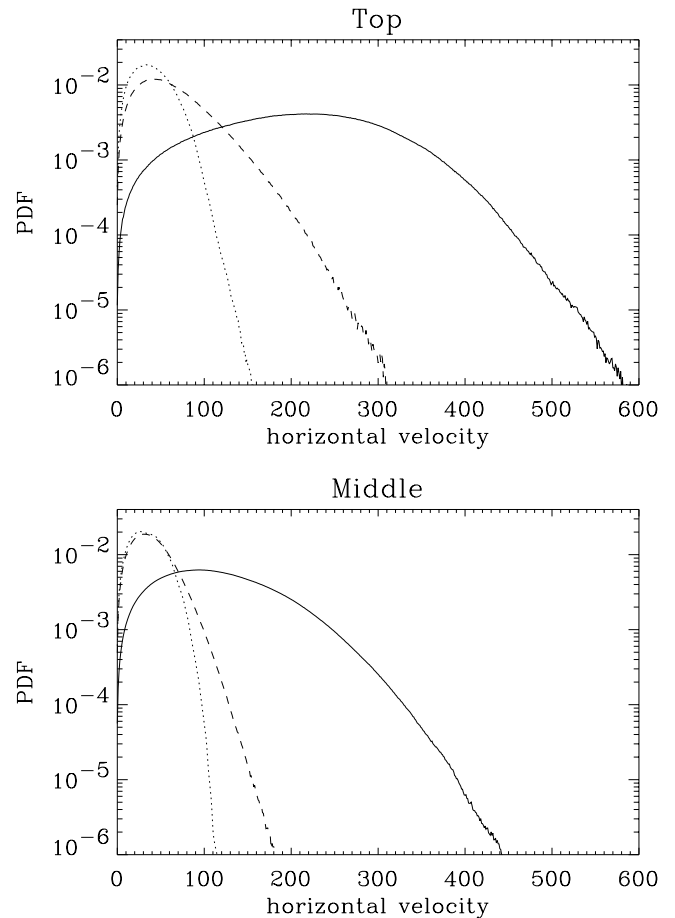


FIG. 13.—Same as Fig. 12, but showing PDFs of the signed velocity field, $|\mathbf{u}| \times \text{sgn } u_z$. These profiles show Gaussian behavior, differing from the corresponding profiles for the magnetic field.

boundary, with isolated cell centers and connected lanes of *down*-flowing fluid, must have a complementary pattern at the lower boundary, with connected lanes of *up*-flowing fluid. In order for the two patterns to coexist, they must be staggered with respect to each other, with the cellular centers of one pattern corresponding to the cellular corners of the other. This interlocking of the two patterns is commonly referred to as *duality*. Since the magnetic field is swept to the cellular boundaries, the upper and lower magnetic networks themselves must also display this dual character. This property is illustrated in Figure 14, where we superpose the magnetic patterns at the upper and lower boundaries. Each pattern is represented by a single color shade—light for the upper boundary, dark for the lower one—irrespective of polarity. The dual nature of the patterns is clearly apparent. It should be noted that even though the convection is strongly time-dependent and the patterns evolve in time, the dual property is preserved.

The duality between the upper and lower magnetic networks leads to an interesting consequence for the intense magnetic structures preferentially located at the cellular corners. Namely, they cannot be monolithic tubelike objects that extend over the entire depth of the layer, for then the strong magnetic fields at the cellular corners of one pattern would emerge as strong magnetic fields at the cellular centers of the other pattern, something that is never seen. In

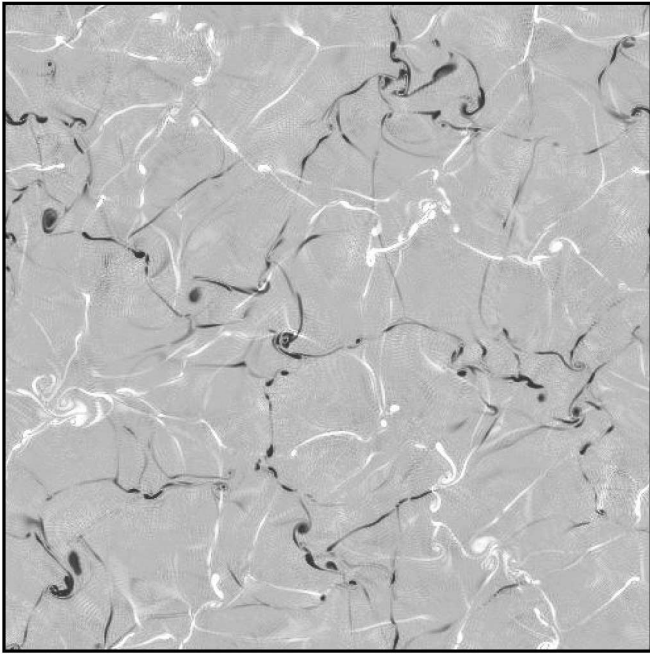


FIG. 14.—Gray-scale plot of the distribution of $|B_z|$ for the dynamo solution (case 0) at the top and bottom of the layer. Light shades denote strong fields of either polarity at the upper boundary, while dark shades correspond to strong fields at the lower boundary. The interlocking mesocellular patterns demonstrate the duality caused by the up-down symmetry of Boussinesq magnetoconvection.

fact, the field lines belonging to a strong magnetic structure at a cellular corner at the upper boundary, say, must connect across to the corresponding corners in the dual pattern at the lower boundary. The resulting complicated magnetic field configuration is illustrated in Figure 15, which shows a volume rendering of the region of intense magnetic field. Although this figure does not actually follow the field lines, it does show the complex connectivity between regions of strong field.

5. DISCUSSION

This is the first systematic study of highly nonlinear three-dimensional magnetoconvection in the Boussinesq approximation. We have taken a fixed Rayleigh number ($Ra = 5 \times 10^5$) in a sufficiently wide box (aspect ratio $\lambda = 10$). If the magnetic field is everywhere set to zero, the fluid convects vigorously, with a Reynolds number $Re = 245$, which would correspond to a magnetic Reynolds number $Rm = 1225$. Once a minute a seed field is inserted, the flow acts as a turbulent dynamo, generating a small-scale disordered magnetic field, with no net flux through the box, whose energy rises until it saturates at a level that is 20% of the (reduced) kinetic energy (Cattaneo 1999). We have explored the effects of imposing a net vertical magnetic flux ($B_0 \lambda^2$) across the box, as B_0 is increased from a tiny value (corresponding to a magnetic energy that is only 1% of the kinetic energy in the field-free case) up to a value that is almost strong enough to halt convection.

In the strong-field regime we find mildly nonlinear behavior associated with oscillatory convection. The individual cells are narrow and vertically elongated, with a characteristic diameter that is about 70% of the layer depth. Flow

across the field is inhibited, and the field lines are only slightly distorted from the vertical, with a correspondingly small increase in magnetic energy, comparable to the kinetic energy of the motion. Weakly nonlinear behavior in this regime can be treated analytically (Clune & Knobloch 1994), while Julien, Knobloch, & Tobias (1999) have developed an asymptotic treatment that is valid in the limit as $Q \rightarrow \infty$ with $Ra = O(Q)$. With a wide computational box we find that such ordered patterns are complicated by the effects of a large-scale two-dimensional flow in cases 6 and 7.

The oscillations give way to chaotic overturning motion in the weak-field regime, and the cell diameter increases gradually as B_0 is reduced. Now the motion becomes strong enough to sweep the magnetic field aside and to concentrate magnetic flux into a network that encloses the rising plumes as they impinge on the upper boundary—with a complementary network that surrounds the sinking plumes at the base of the layer. The patterns found for cases 5, 4, and 3 in Figures 5 and 6 are characteristic of nonlinear magnetoconvection in the intermediate regime, in which the magnetic energy remains significantly greater than the kinetic energy.

Next comes the convective regime, where the magnetic energy is comparable to, or slightly smaller than, the kinetic energy. Now the magnetic pattern begins to show signs of a larger mesocellular flow.

The final transition is from magnetoconvection to the regime in which the imposed field is very weak. Then convection acts as a turbulent dynamo, generating a disordered field whose magnetic energy is greater than that produced merely by amplification of B_0 . Although this regime exists over a finite range in B_0 , we have not presented any examples with positive B_0 , since they would be virtually indistinguishable from case 0. Our main result is that this last transition is smooth.

There have been several investigations of three-dimensional compressible magnetoconvection with large aspect ratio at Rayleigh numbers lower than that considered here. Weiss et al. (2002) carried out a systematic survey of magnetoconvection in a strongly stratified layer and identified transitions from ordered planforms to complicated spatiotemporal behavior as Q was decreased for a fixed Rayleigh number $Ra = 10^5$. They found a transition from a magnetically dominated regime, with steady overturning convection in narrow hexagonal cells, to one with broad and vigorous chaotic plumes, which subsequently amalgamated leading to the phenomenon of flux separation (Tao et al. 1998). In this regime magnetic flux is excluded from the actively convecting regions (which contain clusters of expanding plumes) and concentrated into regions with fields that are locally strong enough to enforce small-scale convection. Flux separation is a robust effect that occurs over a significant range in Q . Since the density drops where fields are locally extremely strong, it becomes increasingly difficult to compute solutions for small Q . There is every reason to expect, however, that there would be a further transition to small-scale dynamo action when Ra is large and B_0 is very weak.

Although flux separation is not seen in any of our Boussinesq calculations, it has been found over a narrow parameter range near the onset of convection (P. C. Matthews 2002, private communication). Apparently, it occurs more readily for compressible convection in deep layers, when the up-down symmetry of our problem is

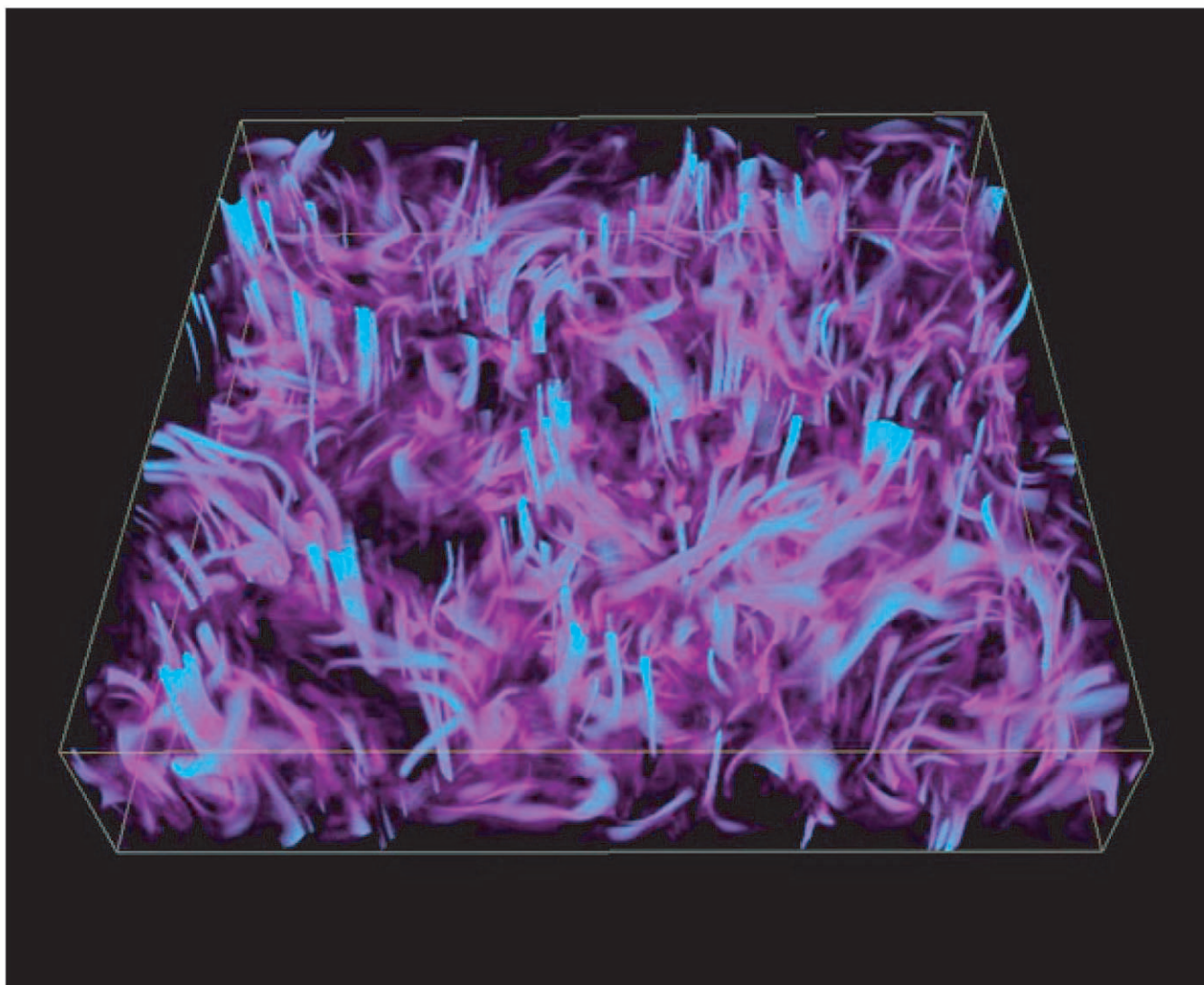


FIG. 15.—Snapshot showing the three-dimensional structure of the strong magnetic component of the magnetic field for the dynamo solution illustrated in Fig. 14. The volume rendering shows only the regions with intense fields (strength more than 50% above the equipartition value, i.e., $|\mathbf{B}| > 300$). These complicated structures link the dual patterns in Fig. 14.

broken and flux is swept aside by rising and expanding plumes. There is also an analogous effect near the onset of convection, when an isolated plume (or “convecton”) can form in a Boussinesq layer that is otherwise stable (Blanchflower 1999; Blanchflower & Weiss 2002).

The different regimes that we have described can be related to interactions between stellar magnetic fields and convection. In Ap stars the ionization of hydrogen and helium can drive convection, which although vigorous, does not contribute significantly to transporting energy. The measured fields are strong enough to suppress this turbulent convection and thus permit the development of the abundance anomalies that are detected spectroscopically (Mestel 1999). The situation is different in late-type stars like the Sun, where energy has to be carried by convection, and the superadiabatic gradient rises until this can occur. Thus, sunspot umbrae correspond to the strong-field regime, where the pattern of convection is dominated by the presence of a strong and almost vertical magnetic field. Plage regions, where the pattern of convection is distorted by magnetic fields, belong to the weak-field regime, and there is a further

transition to the intergranular fields that manifest themselves in *G*-band images as isolated bright points (see, e.g., Berger & Title 1996). Note, however, that isolated flux tubes are not seen in either Boussinesq or compressible calculations; instead, the magnetic flux percolates through the intergranular network, forming strong local fields from time to time.

Photospheric and subphotospheric convection in the Sun is highly turbulent with a magnetic Reynolds number $Rm \geq 10^6$. Thus, one should expect to find dynamo action leading to the generation of small-scale fields. The flux that emerges as ephemeral active regions to form a “magnetic carpet” (Title 2000) is apparently unrelated to the fields that appear more systematically in active regions and sunspots. Bipolar features, with fluxes of the order of 3×10^{18} Mx, emerge near the centers of supergranules. As their footpoints move apart, they split into smaller intergranular flux elements, of the order of 10^{17} Mx, which migrate into the supergranular network, where oppositely directed fields can merge and reconnect (Simon, Title, & Weiss 2001). We suggest that these features owe their origin to small-scale

dynamo action in the outer part of the convection zone. Since photospheric convection shreds the emerging bipole into smaller flux elements that reconnect at supergranule boundaries, it seems unlikely that motion on the scale of granulation could amalgamate those elements to reconstitute a larger bipole. So the small-scale dynamo apparently involves larger scale convection at some deeper level. That leaves open the possibility that granular convection generates magnetic fields on a smaller scale, perhaps associated with the weak but omnipresent fields that can be detected through the Hanle effect (Stenflo, Keller, & Gandorfer 1998).

Computing power has now advanced to a stage where numerical experiments at high Rayleigh numbers and with large aspect ratios can reproduce features that may be compared with those revealed by current observations on the Sun. In the future, more ambitious computations will be

carried out. At the same time, as new telescopes are deployed in space and on the ground, it will become possible to resolve yet finer structures on the solar surface. So we may expect to gain a much clearer understanding of the complex interactions between magnetic fields and convection in our local star.

We have benefitted from conversations with Nicholas Brummell, David Hughes, Michael Proctor, Robert Rosner, Jean-Claude Thelen, and Steven Tobias. Special thanks go to A. Dubey for her help in developing the code and to the supercomputing support staff at NASA Goddard Space Flight Center for their help in running it. We would like to acknowledge the NASA SR&T program at the University of Chicago (F. C. and T. E.) and the PPARC (N. O. W.) for their partial support.

APPENDIX

The basis for the numerical work of the present paper is a Fourier pseudospectral code designed to work efficiently on machines with parallel architecture. Although pseudospectral codes have been used for incompressible fluid dynamics since the late 1970s (Gottlieb & Orszag 1977), parallel versions of these codes are still not commonplace. For this reason, we provide in this appendix a brief outline of the code's structure. Not all the procedures we describe are new, but we nevertheless believe that others will find it useful to have them summarized here.

The starting point for a pseudospectral solver is the relation between a function defined in *configuration* space on a set of $N_x \times N_y \times N_z$ collocation points and its *phase* space representation generated by the discrete Fourier transform (DFT). For functions satisfying the boundary conditions (eq. [8]), this relation takes the form

$$f(x, y, z) = \sum_{n_1} \sum_{n_2} \sum_{n_3} \hat{f}(n_1, n_2, n_3) \exp i(k_1 x) \exp i(k_2 y) \phi^p(k_3 z) + \text{cc} , \quad (\text{A1})$$

where “cc” stands for complex conjugate,

$$k_1 = \frac{2\pi n_1}{\lambda}, \quad k_2 = \frac{2\pi n_2}{\lambda}, \quad k_3 = \pi n_3 , \quad (\text{A2})$$

and $p = \pm 1$, with $\phi^{+1}(s) = \cos s$ and $\phi^{-1}(s) = \sin s$. Here n_1, n_2 , and n_3 are integers in the ranges

$$\begin{aligned} 0 &\leq n_1 \leq N_x/2 - 1 , \\ -(N_y/2 - 1) &\leq n_2 \leq N_y/2 - 1 , \\ 0 &\leq n_3 \leq N_z \text{ if } p = +1 , \\ 1 &\leq n_3 \leq N_z - 1 \text{ if } p = -1 . \end{aligned}$$

With this representation, the solution of equations (1)–(4) can be reduced to five basic tasks: evaluation of derivatives, projection onto the space of solenoidal vector functions, time integration, evaluation of products of functions, and calculation of the DFT.

The idea is to carry out the first four tasks in either configuration or phase space, depending on where they are most convenient, and to use the DFT to transform back and forth between the two spaces. In our case, derivatives, time integration, and projections are computed in phase space, while products are evaluated in configuration space.

We illustrate this process by a simple example based on the momentum equation with no forcing (magnetic or otherwise),

$$(\partial_t - \nabla^2)\mathbf{u} = -\nabla p - \nabla \cdot \mathbf{uu} , \quad (\text{A3})$$

with

$$\nabla \cdot \mathbf{u} = 0 . \quad (\text{A4})$$

The first step is to transform equation (A3) into phase space:

$$(\partial_t + k^2)\hat{\mathbf{u}} = -ik\hat{\mathbf{p}} - ik \cdot \hat{\mathbf{m}} , \quad (\text{A5})$$

where $\hat{\mathbf{m}}$ is the DFT of the symmetric, second-rank tensor \mathbf{uu} .

The next step is to realize that the role of the pressure p in an incompressible fluid is to keep the velocity solenoidal. Thus, the pressure can be eliminated from the equations by requiring that the solution in configuration space be a solenoidal vector

function or, equivalently, that in phase space, it be orthogonal to \mathbf{k} . It can easily be verified that the projection operator,

$$P_{lm} = \left(\frac{k_l k_m}{k^2} - \delta_{lm} \right), \quad (\text{A6})$$

has the property that, for any vector u_l , $P_{lm}u_m$ is orthogonal to \mathbf{k} . Thus, we can rewrite equation (A5) in component notation as

$$(\partial_t + k^2)\hat{u}_l = -iP_{ln}k_q\hat{m}_{qn} \quad (\text{A7})$$

(Orszag & Patterson 1972). It is now fully apparent why it is most convenient to evaluate derivatives and projections in phase space. They reduce to simple multiplications by the components of the wavenumber \mathbf{k} .

The next step is to choose a suitable time integration scheme. This is determined partly by accuracy and speed requirements and partly by personal taste. Two popular choices that provide third-order accuracy, and conditional numerical stability, are the third-order Runge-Kutta (RK3) and the three-level Adam-Bashforth (AB3) schemes (Canuto et al. 1987). Both can be implemented equally efficiently, both have comparable storage requirements, and both require a single evaluation of the right-hand side per step. The results presented in the present work were obtained with an AB3 scheme. For an equation of the type

$$\frac{dX}{dt} = F(X), \quad (\text{A8})$$

it can be written as

$$X^{n+1} = X^n + C_0F(X^n) + C_1F(X^{n-1}) + C_2F(X^{n-2}), \quad (\text{A9})$$

where $X^n = X(t + \delta t)$, $X^{n-1} = X(t - \delta t_1)$, and $X^{n-2} = X(t - \delta t_2)$. The coefficients in equation (A9) are given in terms of the present and (two) previous time steps by

$$\begin{aligned} C_0 &= \delta t + \frac{\delta t^2}{\delta t_1 \delta t_2} \left[\frac{\delta t}{3} + \frac{1}{2}(\delta t_1 + \delta t_2) \right], \\ C_1 &= \frac{\delta t^2}{\delta t_1(\delta t_1 - \delta t_2)} \left(\frac{\delta t}{3} + \frac{1}{2}\delta t_2 \right), \\ C_2 &= -\frac{\delta t^2}{\delta t_2(\delta t_1 - \delta t_2)} \left(\frac{\delta t}{3} + \frac{1}{2}\delta t_1 \right). \end{aligned} \quad (\text{A10})$$

In principle, it is possible to apply equation (A9) to equation (A7); however, the resulting scheme would have potentially severe time step constraints for numerical stability owing to the diffusion term on the left-hand side. A much better scheme can be obtained by noting that equation (A7) has the integrating factor $\exp(-k^2 t)$, which allows it to be rewritten as

$$\partial_t \hat{U}_l = -iP_{ln}k_q \hat{M}_{qn}, \quad (\text{A11})$$

where

$$\hat{U} = \hat{u} \exp(-k^2 t), \quad \text{and} \quad \hat{M} = \hat{m} \exp(-k^2 t) \quad (\text{A12})$$

(Canuto et al. 1987). The application of AB3 to equation (A12) now gives a scheme whose numerical stability is solely determined by advective processes, while still remaining third-order accurate.

Clearly, the above scheme can be used to update \hat{u} , provided that the nonlinear term \hat{m} on the right-hand side can be computed. In terms of phase-space coefficients, the DFT of the product of two variables is given by a convolution sum requiring of the order of N^2 operations, where N is the number of Fourier coefficients. The essence of a pseudospectral method is to replace these sums by fast Fourier transforms (FFTs) and configuration space products that only require of the order of $N \log_2 N$ operations. The idea is that whenever the product of two variables is required, the two variables are transformed into configuration space by FFTs, then they are multiplied, then the product is transformed back into phase space by the inverse FFT.

The first four tasks are all local, not requiring any communication between “distant” subsets of the variables. Thus, their implementation in a parallel environment is trivial since the data subsets in each processor do not need to be communicated to other processors. The calculation of the FFT, however, is not of this type. Each Fourier coefficient depends on the value of the function at all the configuration space points. Thus, the implementation of the FFT in a parallel environment requires some thought. There are two basic approaches: one is to distribute the FFT *across* the processors; the other is to evaluate the FFT *within* the processors and to transpose the data. Timing comparisons (A. Dubey 2002, private communication) suggest that for the typical machine with distributed memory (Linux cluster, IBM SMP, Cray T3E, etc.), the transpose method is the more efficient. We now briefly describe how it is implemented in our code.

We consider the forward FFT (configuration-to-phase) of the three-dimensional variable $U(x,y,z)$, where x , y , and z are *discrete* independent variables corresponding to the values of the collocation points. It is convenient to visualize this data as a cube of values with dimensions N_x , N_y , and N_z . In order to transform the data to phase space, we need to execute one-dimensional transforms along all three directions. Since the plan is to carry out each one-dimensional transform within the processors, we must distribute the data among the processors in at most two directions. This corresponds to cutting the original cube of data into a set of identical rectangular columns. In our specific implementation, the data are distributed

among p_1 processors along the y -direction and among p_2 (typically 2 or 4) processors along the z -direction. Thus, within each processor the configuration space data consist of columns with dimensions N_x , N_y/p_1 , and N_z/p_2 . The full FFT consists of five basic steps: a real-to-complex FFT in the x -direction, where each processor carries out $(N_y N_z)/(p_1 p_2)$ transforms of (real) length N_x ; a “transpose,” whereby the ordering of the indexes becomes y, z, k_1 , and the y -direction is not distributed; a complex-to-complex FFT in the y -direction, where each processor carries out $(N_x N_z)/(2p_1 p_2)$ transforms of (complex) length N_y ; a “transpose,” whereby the ordering of the indexes becomes k_2, z, k_1 , and the z -direction is not distributed; and a sine/cosine transform in the z -direction, where each processor carries out $(N_x N_y)/(p_1 p_2)$ transforms of (real) length N_z .

We should note the following points. There is no interprocessor communication during the FFTs. All the communications are related to the transposes. These consists of a local rearrangement of the data within each processor, plus an interchange of data with another processor. The combined effect of the transposes is to scramble the data, not unlike what happens to the color tiles in a Rubik’s cube. For instance, at the end of a forward FFT, the data in phase space can once again be visualized as a cube but with the ordering k_2, k_3 , and k_1 and with the k_2 -direction distributed among p_2 processors, the k_3 -direction *not* distributed, and the k_1 -direction distributed among p_1 processors. The inverse FFT (phase-to-configuration) is effected by carrying out the inverses of each operation in reverse order. The efficiency of the FFT is paramount for the overall code performance. It can be easily calculated that the pseudospectral solution of equation (1)–(4) requires seven inverse FFTs (θ , plus three components of \mathbf{u} , plus three components of \mathbf{B}), and 12 forward transforms (three components of $\theta\mathbf{u}$, plus six components of the symmetric tensor $\mathbf{uu} - \mathbf{BB}$, plus three components of the antisymmetric tensor $\mathbf{uB} - \mathbf{Bu}$). With a total of 19 FFTs per step, the code practically spends most of its time computing FFTs.

We conclude this appendix with some resolution and timing considerations. All the simulations described in this paper were carried out with a resolution of $512 \times 512 \times 97$ collocation points. We found this to be adequate to resolve all the boundary layers and to give an accurate representation of each variable with a discernible and well-resolved dissipative subrange. Most of the calculations were carried out on the NASA Cray T3e at Goddard Space Flight Center, where, on 128 processors, the code took approximately 5.7 s step^{-1} . With a bigger calculation, using $1024 \times 1024 \times 97$ collocation points, the code was run with up to 1024 Cray T3e processors and showed almost perfect scaling. By contrast, on a 16 processor Linux cluster with 1.7 MHz chips and dedicated Gigaset network a $512 \times 512 \times 97$ calculation took approximately 20 s step^{-1} . However, we observed a substantial deterioration of scaling with more than 16 processors.

REFERENCES

- Berger, T. E., & Tittle, A. M. 1996, *ApJ*, 463, 365
 Blanchflower, S. M. 1999, *Phys. Lett. A*, 261, 74
 Blanchflower, S. M., & Weiss, N. O. 2002, *Phys. Lett. A*, 294, 297
 Brandenburg, A., Jennings, R. L., Nordlund, A., Rieutord, M., Stein, R. F., & Tuominen, I. 1996, *J. Fluid Mech.*, 306, 325
 Canuto, C., Hussaini, M. Y., Quarteroni, A., & Zang, T. A. 1987, *Spectral Methods in Fluid Dynamics* (New York: Springer)
 Cattaneo, F. 1999, *ApJ*, 515, L39
 Cattaneo, F., Lenz, D., & Weiss, N. O. 2001, *ApJ*, 563, L91
 Chandrasekhar, S. 1961, *Hydrodynamic and Hydromagnetic Stability* (Oxford: Clarendon)
 Clune, T., & Knobloch, E. 1994, *Physica*, 74D, 151
 Dorch, S. B. F., & Nordlund, A. 2001, *A&A*, 365, 562
 Emonet, T., & Cattaneo, F. 2001, *ApJ*, 560, L197
 Emonet, T., Cattaneo, F., & Weiss, N. O. 2001, in *Dynamo and Dynamics: A Mathematical Challenge*: ed. P. Chossat, D. Armbruster, & I. Oprea (Dordrecht: Kluwer), 173
 Gottlieb, D., & Orszag, S. A. 1977, *Numerical Analysis of Spectral Methods: Theory and Applications* (Philadelphia: SIAM-CBMS)
 Julien, K., Knobloch, E., & Tobias, S. M. 1999, *Physica*, 128D, 105
 Meneguzzi, M., & Pouquet, A. 1989, *J. Fluid Mech.*, 205, 297
 Mestel, L. 1999, *Stellar Magnetism* (Oxford: Clarendon)
 Nordlund, A., Brandenburg, A., Jennings, R. L., Rieutord, M., Ruokolainen, J., Stein, R. F., & Tuominen, I. 1992, *ApJ*, 392, 647
 Orszag, S. A., & Patterson, G. S., Jr. 1972, *Phys. Rev. Lett.*, 28, 76
 Proctor, M. R. E., & Weiss, N. O. 1982, *Rep. Prog. Phys.*, 45, 1317
 Rucklidge, A. M., Weiss, N. O., Brownjohn, D. P., Matthews, P. C., & Proctor, M. R. E. 2000, *J. Fluid Mech.*, 419, 283
 Schüssler, M. 2001, in *ASP Conf. Ser. 236, Advanced Solar Polarimetry: Theory, Observation, and Instrumentation*, ed. M. Sigwarth (San Francisco: ASP), 343
 Simon, G. W., Tittle, A. M., & Weiss, N. O. 2001, *ApJ*, 561, 427
 Stein, R. F., Bercik, D., & Nordlund, A. 2003, *Nuovo Cimento*, in press
 Stein, R. F., & Nordlund, A. 2003, in *IAU Symp. 210, Modelling of Stellar Atmospheres*, ed. N. E. Piskunov, W. W. Weiss, & D. F. Gray (San Francisco: ASP), in press
 Stenflo, J. O. 1999, in *Second Solar Polarization Workshop: Solar Polarization*, ed. K. N. Nagendra & J. O. Stenflo (Dordrecht: Kluwer), 1
 Stenflo, J. O., Keller, C. U., & Gandorfer, A. 1998, *A&A*, 329, 319
 Stix, M. 2002, *The Sun: An Introduction* (2d ed; Berlin: Springer)
 Tao, L., Weiss, N. O., Brownjohn, D. P., & Proctor, M. R. E. 1998, *ApJ*, 496, L39
 Thelen, J.-C., & Cattaneo, F. 2000, *MNRAS*, 315, L13
 Tittle, A. M. 2000, *Philos. Trans. R. Soc. London, A*, 358, 657
 Tittle, A. M., Topka, K. P., Tarbell, T. D., Schmidt, W., Balke, C., & Scharmer, G. 1992, *ApJ*, 393, 782
 Tobias, S. M., Brummell, N. H., Clune, T. L., & Toomre, J. 1998, *ApJ*, 502, L177
 ———, 2001, *ApJ*, 549, 1183
 Weiss, N. O., Proctor, M. R. E., & Brownjohn, D. P. 2002, *MNRAS*, 337, 293